Received 28 July 2025; accepted 11 August 2025. Date of publication 13 August 2025; date of current version 2 September 2025.

Digital Object Identifier 10.1109/OJCOMS.2025.3598602

Doppler Estimation and Compensation Techniques in LoRa Direct-to-Satellite Communications

JAMIL FARHAT [1], GIANNI PASOLINI [2,3] (Member, IEEE), ENRICO PAOLINI [2,3] (Senior Member, IEEE), MUHAMMAD ASAD ULLAH [4] (Member, IEEE), AND RICHARD DEMO SOUZA [5] (Senior Member, IEEE)

[1]Graduate Program in Electrical and Computer Engineering (CPGEI), Federal University of Technology-Paraná (UTFPR), Curitiba 80230-901, Brazil
[2]CNIT-WiLab, University of Bologna, 40126 Bologna, Italy
[3]Department of Electrical, Electronic, and Information Engineering, University of Bologna, 40126 Bologna, Italy
[4]VTT Technical Research Centre of Finland Ltd., 02044 Espoo, Finland
[5]Department of Electrical and Electronics Engineering, Federal University of Santa Catarina, Florianópolis 88040-900, Brazil

CORRESPONDING AUTHOR: J. FARHAT (e-mail: jamilfarhat@utfpr.edu.br)

This work was supported in part by the Coordination for the Improvement of Higher Education Personnel–CAPES (ROR Identifier: 00x0ma614) for the Article Processing Charge for the Publication of this Research; in part by the Brazil by CNPq under Grant 305021/2021-4; in part by CAPES/STIC-AMSUD under Grant 88881.985542/2024-01; and in part by RNP/MCTI Brasil 6G under Grant 01245.020548/2021-07.

ABSTRACT Within the Low-Power Wide Area Network (LPWAN) framework, the Long Range (LoRa) modulation adopted by Long Range Wide Area Network (LoRaWAN) technology has garnered significant interest as a connectivity solution for Internet of Things (IoT) applications due to its ability to offer low-cost, low-power, and long-range communications. One emerging use case of LoRa is direct-to-satellite (DtS) connectivity, which extends coverage to remote areas for supporting IoT operations. The satellite IoT industry mainly prefers Low Earth Orbit (LEO) because it has lower launch costs and less path loss compared to Geostationary orbit. However, a major drawback of LEO satellites is the impact of the Doppler effect caused by their mobility. Earlier studies have confirmed that the Doppler effect significantly degrades the LoRa DtS performance. In this paper, we propose four frameworks for Doppler estimation and compensation in LoRa DtS connectivity and numerically compare the performance against the ideal scenario without the Doppler effect. Furthermore, we investigate the trade-offs among these frameworks by analyzing the interplay between spreading factor, and other key parameters related to the Doppler effect. The results provide insights into how to achieve robust LoRa configurations for DtS connectivity.

INDEX TERMS Direct-to-satellite, LEO, LoRa, LPWAN.

I. INTRODUCTION

THE Internet of Things (IoT) is a transformative paradigm and a cornerstone of massive Machine-Type Communications (mMTC), designed to connect a vast number of devices, typically (though not exclusively) characterized by low-power consumption and low-data-rates [1]. Its applications span diverse sectors, including industrial automation, precision agriculture, environmental monitoring, transport & logistics, and smart cities [2], [3]. However, each of these domains presents distinct challenges, necessitating scalable solutions that address constraints on power consumption, device complexity, cost-efficiency, and data rates [4], [5].

To address the need for long-range, low-power connections, both 3GPP and non-3GPP Low-Power Wide Area Networks (LPWANs) have emerged as key technologies within the IoT ecosystem, offering a trade-off between energy efficiency, coverage, data rate, and deployment cost. Their capability to provide long-range connectivity makes them particularly well-suited for large-scale IoT deployments across diverse environments [6], [7], [8], [9].

Among non-3GPP LPWAN technologies, LoRaWAN has established itself as a leading connectivity solution for IoT applications [7], [10]. A key factor behind its success is its use of Long Range (LoRa) chirp spread spectrum (CSS) modulation, developed and patented by Semtech [11], which enables dynamic adaptation to varying channel conditions. This flexibility allows for a trade-off between data rate and receiver sensitivity, allowing for optimized performance across a wide range of applications and coverage areas [12].

In particular, LoRaWAN is widely used for long-range communication and is increasingly considered for integration into satellite-based mMTC networks [13], providing a cost-effective path to global coverage [4].

Notably, LEO satellites have demonstrated strong potential for supporting LoRa DtS communications, not only extending coverage to remote areas but also serving as a resilient backup for terrestrial networks by interconnecting LoRaWAN gateways through satellite backhaul [14], [15], [16]. However, for this approach to be truly effective, a significant challenge must be addressed: the high orbital velocity of LEO satellites. To prevent falling back to Earth due to gravitational attraction, they must travel at speeds much faster than the Earth's rotational speed. This results in considerable relative motion between the satellite and terrestrial IoT devices, which leads to time-varying shifts in the carrier frequency of the transmitted signal [17]. The rate at which this frequency changes, referred to as the Doppler rate, depends on the satellite's trajectory, and the relative position of the transmitter and receiver, directly impacting signal synchronization and communication reliability.

Such a dynamic behavior introduces significant difficulties, as both the Doppler shift and the Doppler rate vary over time, requiring the receiver to continuously adjust to these changes to maintain reliable communication and therefore presenting unique challenges for the physical layer of LoRa receivers [18], [19]. It is worth noting, in this regard, that the Doppler shift primarily affects the beginning and end of the satellite's visibility window, causing significant variations in the carrier frequency at these points [17]. In contrast, the Doppler rate has the most noticeable impact during the middle of the visibility window [17]. The combined effect of both phenomena leads to packet losses which further reduces the effective visibility duration.

This work aims to extend the effective communication window by mitigating Doppler-related impairments, thereby increasing the number of available transmission opportunities for IoT devices. As a result, it enhances not only the performance of the modulation scheme but also the overall efficiency of the network.

A. NOVELTY AND CONTRIBUTIONS

In the context of satellite communications, there are two primary access modes: indirect-to-satellite (ItS) and DtS. In the ItS mode, an intermediary terrestrial gateway is required to facilitate communication between the satellite and the terrestrial IoT device. This intermediary gateway typically acts as a relay, forwarding the data between the IoT device and the satellite. Conversely, DtS mode allows IoT devices to communicate directly with satellites, removing the dependency on ground-based infrastructure and thereby simplifying network deployment [15], [20]. This makes DtS a preferred solution for achieving global coverage.

In this paper, we present and discuss strategies for estimating and compensating for Doppler-related impairments at the satellite, with the goal of enhancing the performance of LoRa DtS systems. Specifically, our contributions consist of four strategies, each utilizing specific chirps within the LoRa frame as pilots to estimate the Doppler effect. These solutions potentially offer increasing accuracy, each addressing the challenge through distinct methods: *i) point* estimation, which uses the last downchirp in the LoRa frame structure to estimate the Doppler shift; *ii) linear* estimation, which also calculates the angular coefficient of Doppler shift variations over time by comparing the first and last downchirps within the LoRa frame; and *iii) midamble* based estimations, which build upon the linear and point estimation by refining them at specified intervals, further improving accuracy.

It is important to emphasize that these solutions require no complex computations, and their implementation relies solely on software/firmware updates. Each strategy is carefully evaluated using numerical simulations that examine their performance under different Doppler scenarios. The results highlight the trade-offs between error rates and compensation accuracy, providing valuable insights into their feasibility in real-world deployments of LoRa DtS systems. In summary, the main contributions of this work are as follows:

- We propose and evaluate four Doppler estimation approaches, point, linear, midamble-point, and midamble-linear, and analyze their effectiveness in improving compensation accuracy and reducing error rates.
- We compare the trade-offs between these approaches through detailed numerical simulations, highlighting their relative strengths and weaknesses in mitigating Doppler effects in LoRa DtS communication systems.
- We demonstrate, by numerical results, that the midamble-point-based estimation approach delivers consistent performance, performing nearly as well as the best approach under various conditions, including different signal-to-noise ratio (SNR) levels, payload lengths, and satellite positions. Additionally, we analyze the optimal midamble update interval to improve error performance.
- Our results underscore the critical importance of selecting appropriate Doppler estimation strategies based on key LoRa parameters, such as the spreading factor and the interplay between Doppler shift, signal configuration, and system constraints.

The remainder of this paper is organized as follows. Section II presents the state-of-the-art in related research. Section III provides an overview of the key characteristics of LoRa signals, including the frame structure, while Section IV introduces fundamental concepts related to Doppler effects. Following this, Section V examines the impact of Doppler effects on LoRa DtS communications. Section VI introduces the proposed frameworks for Doppler estimation, outlining strategies to mitigate Doppler shift and rate in satellite-based

systems. Section VII presents the numerical results obtained from simulations, and Section VIII concludes the paper with final remarks.

II. STATE-OF-THE-ART

A. LINK BUDGET AND SCALABILITY ASPECTS

Recent studies have extensively analyzed the performance of LoRa in various contexts, primarily focusing on link budget and scalability aspects [12], [20], [21], [22], [23], [24], [25], [26], [27]. For instance, [21] proposes novel modulation and demodulation techniques to enhance efficiency and performance, with insights into LoRa signal characteristics and demodulation techniques provided in [12], [28]. More recently, a comprehensive overview of CSS modulation, including signal generation, detection, and error performance, is presented in [22], offering a deeper understanding of LoRa's capabilities in IoT networks.

In the context of LoRa DtS networks, advancements in scalability and concurrent uplink transmissions have been explored. For example, [24] introduces a fractional chirp rate-based CSS modulation scheme to enable non-orthogonal multiple access while maintaining noise immunity. Similarly, [25] proposes an ALOHA-based scheme for overloaded LoRa-DtS networks, where devices dynamically adjust transmission rates to optimize performance. Additionally, [26] presents an efficient random access scheme with a preamble structure designed for joint estimation of timing advance and carrier frequency offset, though limited to integer subcarrier spacing shifts. Finally, [27] investigates collision-free uplink transmissions in uncoordinated LEO satellite IoT networks.

In a broader scope, [29] analyzes the technological challenges of Direct-to-Smartphone satellite communications, proposing key solutions like an air interface for high-dynamic scenarios, ultra-large spaceborne multi-beam antennas, and on-demand scheduling of narrow beams for random access. The work in [30] investigates enhancing security in satellite downlink communications by using a satellite-terrestrial integrated network and an absorptive reconfigurable intelligent surface (RIS) to maximize the secrecy rate. Similarly, the use of RIS is investigated in [31] for hybrid satellite-terrestrial relay networks, proposing a joint beamforming design to minimize total transmit power while ensuring user rate requirements. Finally, to address long transmission distances and limited spectrum, [32] proposes a space-aerial-terrestrial relay network using a hybrid-free space optical/radio frequency mode optimized via an access-free federated deep reinforcement learning framework.

Although these studies collectively demonstrate the feasibility of LoRa, DtS, and satellite networks, Doppler effects remain an open challenge. In particular, while significant progress has been made in improving the link budget and scalability, further research is needed on how to estimate and compensate for Doppler shift and Doppler rate in LEO satellite communications.[1]

B. DOPPLER ASPECTS

Doppler effects in LoRa-based satellite communication have also been widely studied through field trials, laboratory experiments, real-world flight tests, and analytical models. In [34], an experimental setup is presented where a software-defined radio (SDR) emulates Doppler effects on a LoRa satellite link operating at 868 MHz. The study concludes that LoRa technology exhibits high immunity to static Doppler effects, whereas dynamic Doppler effects introduce a higher error rate.

Regarding laboratory and outdoor experiments involving device mobility, the study in [35] investigates a LoRa link in which the end device is mounted on a lathe machine rotating at 1500 rounds per minute, corresponding to an equivalent linear velocity of approximately 80 km/h. In [36], a LoRa end device was instead installed on a vehicle moving at variable speeds ranging from 32 to 104 km/h, causing Doppler shifts between 300 and 400 Hz. Both experiments confirm that LoRa is sensitive to the Doppler effect. This is particularly significant because the Doppler effect caused by vehicular mobility is much lower than that encountered in typical LEO satellite communications, where satellites orbit at approximately $27,000$ km/h.

In [13], [37] laboratory experiments considered a LEO satellite orbiting at altitudes of 200 km and 550 km, operating in the 430 MHz-434 MHz frequency band. Following these experiments, these works resulted in the development of LoRa satellite named Norby, which was launched on September 28, 2020. Norby carries an on-board SX1278 transceiver and operates at a carrier frequency of 436.703 MHz. At the time of writing this paper, approximately one million LoRa packets from Norby have been successfully received by multiple terrestrial gateways. Moreover, over 21 million telemetry packets from various LoRa satellites have been successful received by terrestrial LoRaWAN gateways. This impressive milestone confirms the feasibility of LoRa DtS communications [38]. Moreover, the Norby mission provided valuable insights into the limitations of CSS modulation in LEO satellite communications. Particularly, the initial Norby flight-test experiments, described in [39], helped understanding the limitations of LoRa modulation at 436.703 MHz and an orbital altitude of 560 km. These experiments used a variety of configurations, including bandwidths $B \in \{31.25, 62.5, 125, 500\}$ kHz and payload sizes of 55 and 143 bytes. With such parameters, twenty experiments, each corresponding to a unique configuration, were conducted to investigate the impact of Doppler effect on LoRa robustness.

[1] While significant advancements have been made in Doppler compensation for Non-Terrestrial Networks within 3GPP standards, our paper focuses on LoRa systems. LoRa operates under distinct design principles, prioritizing ultra-low power consumption, simplicity, and cost-effectiveness [33], unlike the typically more complex 3GPP technologies.

Similar to terrestrial LoRa studies [35], [36] and LoRa DtS laboratory experiments [13], [37], the Norby experiments described in [39] confirm LoRa's immunity to the Doppler effect only for a limited set of configurations. Additionally, the flight-test experiments provided valuable insights into the distinct roles played by Doppler shift and Doppler rate in affecting link reliability and demodulation performance. Particularly, these experiments led to the following key findings:

- the Doppler shift degrades LoRa signal reception and causes communication failure at the lowest elevation angles, which correspond to the maximum link distance and the highest Doppler shift;
- the Doppler rate challenges the receiver's frequency tracking loop and causes communication failure at high elevation angles, which typically corresponds to minimum link distance, where the Doppler rate reaches its highest value (in absolute terms).

As examined in [17], [39], at a 90 degree elevation angle, the Doppler shift is almost 0 kHz, presenting no challenges to successful signal reception. However, at the same 90 degree elevation, there is a very high Doppler rate which challenges the LoRa packets with high time-on-air. This makes LoRa modulation particularly vulnerable when configurations that increase the transmission duration are used.

Several approaches have been proposed to mitigate Doppler-induced impairments in LoRa systems. The work in [40], for instance, introduces a receiver architecture that uses preamble symbols for Doppler estimation and compensation. While this research served as an important inspiration, its investigation does not explore the potential of the built-in Low Data Rate Optimization (LDRO) mode,[2] which, as our results show, offers distinct advantages under high Doppler conditions. A similar preamble-based frequency offset estimation is proposed in [41], but its focus on terrestrial communications does not address the unique and more severe Doppler challenges inherent to satellite links.

A different strategy is presented in [42], which embeds pilot symbols within the LoRa payload for Doppler estimation and compensation. However, the effectiveness of this method is demonstrated with only a single figure in its numerical results. This prevents a comprehensive assessment of its performance across varying modulation parameters, pilot configurations, Doppler conditions, or with the LDRO mode enabled. A critical limitation common to all these prior works is the absence of a comparative analysis against alternative strategies, making it difficult to ascertain their relative performance and practicality.

[2]The LDRO mode increases a packet's Time-on-Air (ToA), which directly translates to higher energy consumption. Despite this overhead, the mode is a valuable tool for improving robustness against frequency offsets, which are common during the long transmission and reception periods at high spreading factors. This trade-off is crucial in challenging channel conditions, allowing devices to maintain reliable communication where it might otherwise fail and justifying the additional energy cost.

To address these gaps, this paper introduces and systematically evaluates a suite of four distinct Doppler estimation strategies that leverage either preamble or embedded pilot symbols. These approaches employ different techniques to estimate both the initial Doppler shift and its rate of change over the frame duration. Crucially, and in contrast to prior art, we conduct a rigorous comparative analysis of these methods. Their effectiveness is benchmarked across a wide range of conditions, including different modulation parameters, various satellite orbital positions, and with the LDRO mode both enabled and disabled, thereby providing a comprehensive understanding of the trade-offs involved.

III. PRELIMINARIES ON LoRa AND ITS ADOPTION IN DtS COMMUNICATIONS

A. LoRa MODULATION

LoRa is a specialized implementation of the CSS modulation, designed to enable low-power communication, provide high immunity to interference, and facilitate time and frequency synchronization at the receiver. It is based on a set of linear chirps—short-time sinusoids whose frequencies sweep linearly over a given bandwidth B [12], [17]—making it a particular case of frequency modulation with linear frequency deviation. Specifically, LoRa employs M uniquely shaped chirps, each representing a distinct symbol s in the modulation alphabet $\mathcal{S} = \{0, 1, \ldots, M-1\}$.

From a mathematical viewpoint, a chirp can be expressed as [12]

$$c(s,t) = V_0 \cos\left(2\pi F_C t + 2\pi \int_0^t \Delta f(s,\xi)\, d\xi\right),\ 0 \le t \le T_c, \quad (1)$$

where V_0 represents the amplitude, F_C is the center frequency of the sweep interval $[F_C - \frac{B}{2}, F_C + \frac{B}{2}]$, T_c is the chirp duration, and $\Delta f(s,t)$ denotes the instantaneous frequency deviation from F_C, which depends on s and varies within $[-\frac{B}{2}, \frac{B}{2}]$.

More precisely, for each symbol $s \in \mathcal{S}$, the instantaneous frequency deviation $\Delta f(s,t)$ of the corresponding chirp starts at $-\frac{B}{2} + \frac{B}{M}s$ and increases linearly to $\frac{B}{2}$. Upon reaching the maximum offset $\frac{B}{2}$, $\Delta f(s,t)$ wraps around to $-\frac{B}{2}$ and continues to increase linearly until the initial value $-\frac{B}{2} + \frac{B}{M}s$ is reached at $t = T_c$. Fig. 1 illustrates an example of instantaneous frequency deviation with $M = 256$, $s = 91$, $B = 500$ kHz, and $T_c = 5.12 \cdot 10^{-4}$s.

Remarkably, LoRa enables a straightforward trade-off between sensitivity and data rate. This balance is achieved by carefully selecting two key parameters: the bandwidth B and the spreading factor SF. Specifically, increasing the bandwidth—configurable to 125 kHz, 250 kHz, or 500 kHz—enhances the bit rate at the expense of reduced sensitivity. The spreading factor, in turn, ranges from SF = 7 to SF = 12 and influences the chirp duration, ultimately impacting communication reliability. In fact, LoRa is designed to adhere to the relationship $BT_c = M$, with $M = 2^{SF}$. Therefore, for a given bandwidth B, increasing SF leads to a longer chirp duration, thereby enhancing communication reliability.

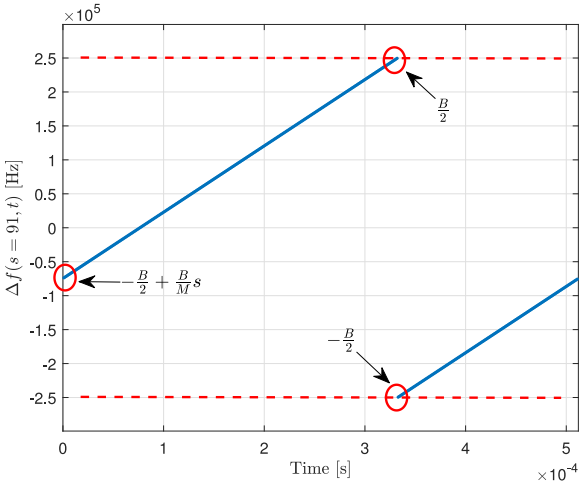

FIGURE 1. Representation of the instantaneous frequency deviation. $s = 91$, $B = 500$ kHz, $T_c = 5.12 \cdot 10^{-4}$ s, with the frequency boundaries highlighted by the dashed red lines.

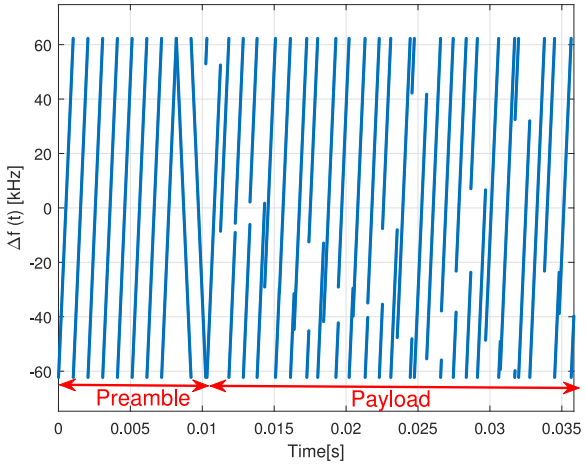

FIGURE 2. Frequency deviation within a LoRa frame. $B = 125$ kHz, SF $= 7$, $T_c = 1$ ms.

This interplay between bandwidth, spreading factor, and symbol duration ensures that LoRa can adapt to different application requirements, establishing it as a successful technology.

B. LoRa DEMODULATION

To provide a clearer understanding of the Doppler estimation strategies introduced in the following sections, we first revisit the LoRa demodulation process, as outlined in [12]. Based on (1), and assuming that in the context of payload demodulation $t = 0$ s represents the start of the payload containing n_{sym} chirps, the chirp corresponding to the n-th data symbol s_n can be expressed as

$$c_n(t) = V_0 \cos[2\pi F_C t + \omega(s_n, t)], \quad nT_c \le t \le (n+1)T_c \quad (2)$$

where $n = \{0, 1, \ldots, n_{\text{sym}} - 1\}$, and $\omega(s_n, t)$ is the phase deviation given by

$$\omega(s_n, t) = 2\pi \int_{nT_c}^{t} \Delta f(s_n, \xi) \mathrm{d}\xi, \quad (3)$$

with $\Delta f(s_n, t)$ representing the instantaneous frequency deviation corresponding to s_n and $nT_c \le t \le (n+1)T_c$. Consequently, the corresponding complex envelope within the n-th symbol interval is given by

$$i_n(t) = V_0 \exp\big[j\omega(s_n, t)\big]. \quad (4)$$

Given (4), a dechirping operation is performed at the receiver by multiplying $i_n(t)$ with the complex conjugate of a pure upchirp,[3] yielding

$$r_n(t) = i_n(t) \exp\big[-j\theta(t - nT_c)\big], \quad (5)$$

where the phase deviation $\theta(t)$ of a pure upchirp is given by

$$\theta(t) = 2\pi \left[-\frac{B}{2}t + \frac{B}{2T_c}t^2 \right], \quad 0 \le t \le T_c. \quad (6)$$

[3]The complex conjugate of a pure upchirp is a pure downchirp, whose frequency deviation decreases linearly from $\frac{B}{2}$ to $-\frac{B}{2}$.

It is important to note that dechirping requires frame synchronization, which can still be achieved even in the presence of Doppler effects [40].

Demodulation is then completed by computing the Fourier transform of (5) and extracting the transmitted symbol s_n from the frequency bin, numbered from 0 to $M - 1$, where the spectrum peak appears. Unfortunately, in the presence of Doppler effect, a frequency shift is introduced, which may lead to symbol misalignment. This highlights the need for effective strategies to estimate and compensate for such frequency deviations, which are the primary focus of this paper. To achieve this, we leverage the structure of the LoRa frame, which is detailed in the following section.

C. LoRa FRAME STRUCTURE

The LoRa frame format consists of several components: a preamble, a frame header (optional), the payload, and optionally a cyclic redundancy check (CRC) to enable error detection. An example is shown in Fig. 2, which illustrates the frequency deviation for a frame consisting of the preamble and the payload, with $B = 125$ kHz and SF $= 7$.

The preamble is crucial for synchronizing the receiver with the transmitted signal and mainly consists of n_{up} pure upchirps. For instance, Fig. 2 illustrates a preamble containing $n_{\text{up}} = 8$ upchirps at the beginning of the frame. Each upchirp has a frequency deviation that increases linearly from $-\frac{B}{2}$ to $\frac{B}{2}$. This sequence of upchirps is followed by n_{dw} downchirps, typically set to $n_{\text{dw}} = 2.25$, marking the end of the preamble and ensuring proper frame synchronization at the receiver.[4] As it is evident in Fig. 2, the frequency deviation of the downchirps decreases linearly, reversing the sweep of the upchirp. The remainder of the frame consists of the payload, which carries the actual data to be transmitted. It is composed of n_{sym} chirps, each representing one symbol from the modulation alphabet $\mathcal{S}$, which encodes

[4]Fig. 2 shows only two downchirps, omitting the incomplete downchirp, as it is not relevant to the discussion in this paper.

TABLE 1. Potential satellite IoT applications and traffic models.

Application	Report period seconds	Payload bytes	ToA [ms] SF = 7	SF = 10	SF = 12
Air traffic (ADS-B)	1	32	92.4	575.5	2138.1
Marine traffic (AIS)	2-180	21	77.1	452.6	1810.4
Vehicle tracking	120	8	56.6	370.7	1482.8
Wildlife tracking	120	10	61.7	370.7	1482.8
Wind turbine	600	10	61.7	370.7	1482.8
Smart meter	900	12	61.7	411.6	1482.8
Smart agriculture	1800	10	61.7	370.7	1482.8

$M = 2^{\mathrm{SF}}$ bits. For example, the payload in the frame shown in Fig. 2 consists of 25 chirps, starting immediately after the preamble downchirps. As discussed in Section III-A, the initial frequency of each chirp in the payload depends on the modulation symbol $s \in \mathcal{S}$ transmitted during the corresponding chirp interval.

In LoRa terminology, the duration of a frame transmission is referred to as the ToA. It is important to note that the ToA depends not only on the number of symbols (i.e., chirps) in the payload, but also on the SF, which determines the duration of each chirp. This is particularly relevant because longer frames, typically associated with higher SFs, are more susceptible to the Doppler rate, which can introduce significant frequency variations between the start and end of a frame.

D. POTENTIAL LoRa DtS APPLICATIONS

Table 1 shows DtS IoT data traffic models including payload size, reporting period, and ToA, considering a bandwidth of 125 kHz, for different applications. For instance, aircraft Automatic Dependent Surveillance–Broadcast (ADS-B) systems transmit 32-byte messages every second. Automatic Identification System (AIS) transmits 21-byte messages every 2 seconds for ships traveling over 23 knots [43], [44], while wind turbine monitoring systems send 10-byte payloads every 600 seconds [16]. In smart agriculture, devices typically transmit 10 bytes every 1800 seconds [45], and smart meters report 12-byte packets at regular intervals. As anticipated in Section III-C, the varying transmission intervals across different applications result in different Doppler effects experienced within each frame.

IV. DOPPLER EFFECT

As previously mentioned, the relative velocity of a terrestrial end device and a LEO satellite introduces significant challenges for DtS communications. To maintain their orbits, LEO satellites move at speeds much higher than the Earth's rotational velocity, resulting in substantial relative velocity with terrestrial IoT devices. As illustrated in Fig. 3, this relative velocity causes an offset between the transmitted carrier frequency F_{C} and the received carrier frequency $F_{\mathrm{R}}(t)$. This phenomenon, called Doppler effect, significantly impacts the physical layer of receivers, posing challenges in signal acquisition, synchronization, and demodulation [18].

Specifically, the Doppler effect consists of two key phenomena: Doppler shift, which refers to the instantaneous frequency change due to relative motion, and Doppler rate,

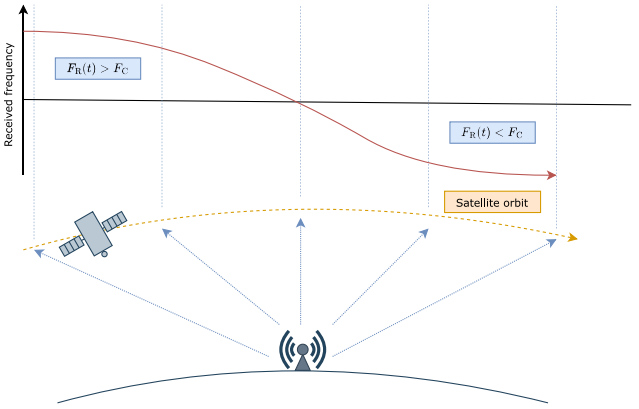

FIGURE 3. Variation of the received carrier frequency, $F_{\mathrm{R}}(t)$, over time due to the satellite's motion along its orbit.

which describes how quickly this frequency shift varies over time. In an ideal end device and satellite geometry, the Doppler shift is most pronounced at low elevation angles, where the distance between the satellite and the IoT device is higher. Conversely, the Doppler rate becomes more significant at high elevation angles, where the satellite is nearly overhead and the link distance is minimal.

Mathematically, the Doppler shift $F_{\mathrm{D}}(t)$ at any given time t is defined as [17]

$$F_{\mathrm{D}}(t) = F_{\mathrm{R}}(t) - F_{\mathrm{C}}, \tag{7}$$

where $F_{\mathrm{R}}(t)$ is the received carrier frequency, which varies over time due to the satellite's motion, and F_{C} is the transmitted carrier frequency. The Doppler shift experienced by the satellite when receiving IoT messages from a terrestrial device is given by

$$F_{\mathrm{D}}(t) = -\frac{v(t)}{c} F_{\mathrm{C}}, \tag{8}$$

where $v(t)$ is the relative velocity[5] of the satellite as seen by an IoT device,[6] and c denotes the speed of light.[7]

On the other hand, the Doppler rate, $\Delta F_{\mathrm{D}}(t)$, is mathematically defined as the time derivative of the Doppler shift:

$$\Delta F_{\mathrm{D}}(t) = \frac{\mathrm{d}F_{\mathrm{D}}(t)}{\mathrm{d}t}. \tag{9}$$

Clearly, both Doppler shift and Doppler rate are highly dependent on the satellite's position, velocity, trajectory as well as on the carrier frequency. As an example, the

[5] $v(t)$ is assumed to be negative, thus generating a positive Doppler shift, when the satellite is moving toward the IoT device. In contrast, if the satellite is moving away from the IoT device, $v(t)$ will be positive, resulting in a negative Doppler shift.

[6] In real scenarios, computing the relative velocity $v(t)$ requires accurate satellite data (position and velocity), precise IoT device location (latitude, longitude, altitude), and time synchronization to correlate received signals with the satellite's position. Obtaining precise data can be challenging, as it often relies on satellite operators or tracking services. Additionally, errors in device positioning or timing can significantly impact the accuracy of $v(t)$.

[7] Equation (8) provides a good approximation of the Doppler shift when $v(t)$ is small compared to c, which holds true in all practical cases.

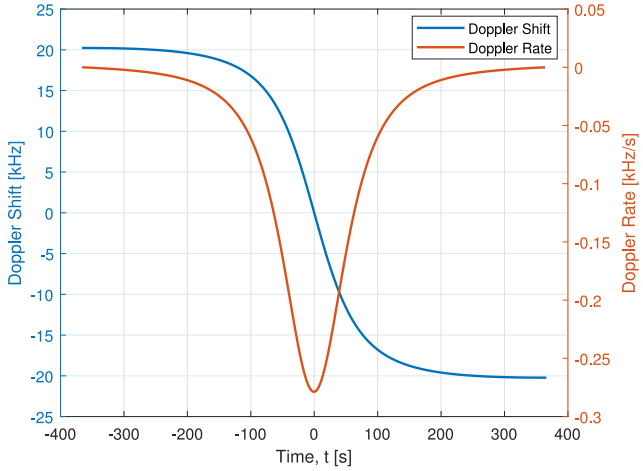

FIGURE 4. The LEO-satellite Doppler Shift and Doppler Rate for an orbital distance of 550 km at a carrier frequency of 868 MHz.

magnitude of both phenomena, derived from the theoretical framework outlined in [13], are illustrated in Fig. 4, considering $F_C = 868$ MHz and a satellite orbital height of 550 km [46]. In this figure, $t = 0$ s corresponds to the instant when the satellite is directly above the IoT device (i.e., at the highest elevation angle), while $t = \pm 366$ s marks the points of lowest elevation angle. As expected, a more pronounced Doppler shift, plotted against the left y-axis, occurs at low elevation angles, whereas the highest Doppler rate, which refers to the right y-axis, is observed at the highest elevation angle.

V. IMPACT OF DOPPLER ON LoRa COMMUNICATIONS

Both Doppler shift and Doppler rate can severely degrade LoRa signal reception, especially when they exceed the receiver's tolerance thresholds. For instance, a high Doppler shift may prevent the receiver from locking onto the carrier frequency, while a high Doppler rate can disrupt carrier synchronization even after it has been established, ultimately leading to frame loss.

Notably, LoRa modulation incorporates a built-in strategy to enhance resistance to Doppler effects through the LDRO mode. For a given SF, this mode reduces the number of bits transmitted per symbol, effectively decreasing the modulation alphabet's cardinality to $M = 2^{\mathrm{SF}-2}$. By lowering symbol density, the frequency separation $\frac{B}{M}$ between chirps increases by a factor of four, thus improving robustness against Doppler.[8] However, this increased robustness comes at the cost of reduced data rates, as fewer bits are mapped to a symbol.

As anticipated in Section III-A, SF is a key parameter in LoRa communication, as it directly influences receiver sensitivity and higher SF values allow for extended transmission distances between the transmitter and receiver. This characteristic is particularly crucial in DtS communication, where long-range connectivity is essential, making higher SFs especially beneficial for enhancing receiver sensitivity.

However, the choice of SF also affects the system's response to the Doppler effect. In particular, as SF increases, the frequency separation between chirps decreases, making the receiver more susceptible to Doppler shift. Additionally, the Doppler shift experienced at the beginning of a received frame differs from that at the end, with its variation depending not only on $\Delta F_D(t)$ but also on the frame duration, i.e., the ToA. Since in LoRa communication the ToA increases with SF, configurations with higher SF are more susceptible to the Doppler effect, as the carrier frequency may change significantly during the reception of the frame. It turns out, therefore, that SF impacts receiver sensitivity and Doppler robustness in opposing ways, highlighting the importance of accurately estimating and compensating for the Doppler effect to ensure reliable communication in DtS scenarios.

To highlight the impact of SF variations under different Doppler conditions, Fig. 5 investigates the Doppler shifts as a function of time for different satellite positions along the orbit and SF values. As an illustrative example, Fig. 5 shows the Doppler shift expected by the receiver over a large time window (approximately 2 seconds) for the lowest and highest SF values, namely SF = 7 and SF = 12. The scenario considers a satellite orbiting at an altitude of 550 km, a carrier frequency $F_C = 868$ MHz, and a payload size of 15 Bytes. The corresponding bit rates, following [22], are given by $R_b = \frac{\mathrm{CR}\,B}{2^{\mathrm{SF}-1}}$, where CR = 1 is the coding rate and $B = 125$ kHz is the bandwidth. For SF = 7, this results in a rate of $R_b \approx 6835$ bits/s, while for SF = 12, the rate reduces to $R_b \approx 366$ bits/s. These values reflect the faster and slower chirping rates associated with low and high SF values, respectively.

- *Case 1:* This scenario corresponds to the satellite's position that yields the maximum Doppler shift, along with a minimum and negative Doppler rate. As shown in Fig. 4, this situation occurs approximately at times $t = -366$ s. This condition results in a substantial yet slowly varying frequency shift caused by the satellite's relative motion.
- *Case 2:* This scenario focuses on the satellite positioned as to experience the maximum Doppler rate with minimal Doppler shift. As shown in Fig. 4, at $t = 0$ s the Doppler rate is at its highest, although the overall Doppler shift remains relatively low.

Specifically, *Case 1* results in higher Doppler shifts (approximately 20 kHz) for both SF = 7 and SF = 12, but with relatively low Doppler rates. In fact, the Doppler shift remains nearly constant at around 20 kHz throughout the entire frame duration. In contrast, *Case 2* exhibits more pronounced Doppler rate effects, particularly for SF = 12, due to its longer ToA. Specifically, for SF = 12, the Doppler shift varies by approximately 510 Hz over the

[8]It is important to note that LDRO mode is mandatory for higher spreading factors (e.g., SF = 11 and SF = 12) when operating at a 125 kHz bandwidth. This requirement arises because the extended frame duration at higher spreading factors makes the system more susceptible to Doppler [47].

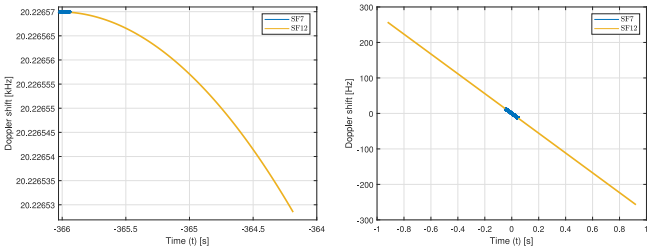

FIGURE 5. Doppler shifts are analyzed for different SF values and satellite positions. The left figure illustrates *Case 1*, while the right figure depicts the Doppler effects for *Case 2* under the same SF values.

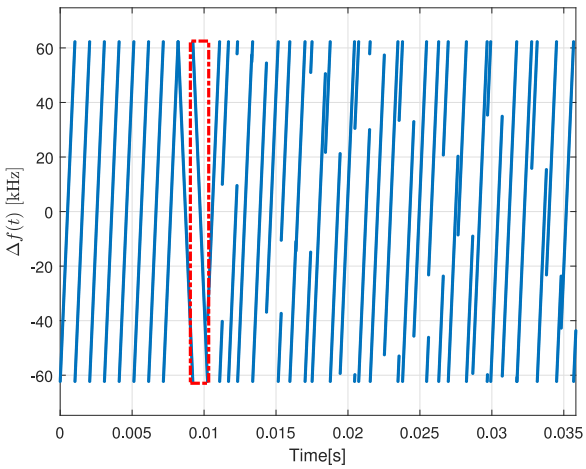

FIGURE 6. Frequency deviation within a LoRa frame with $n_{up} = 8$, $n_{dw} = 2$ and $n_{sym} = 25$. The dotted-dashed red line indicates the last synchronization downchirp used for point Doppler estimation.

frame duration, compared to about 25 Hz for SF = 7. As anticipated, the extended ToA associated with higher SF values increases susceptibility to Doppler effects, as the receiver is more affected by the rapid frequency variations characteristic of *Case 2*.

To address these challenges, robust estimation and compensation techniques are essential for mitigating the Doppler effect. The following section presents four strategies for Doppler estimation and compensation, specifically designed for LoRa DtS links in LEO satellite scenarios.

VI. PROPOSED DOPPLER ESTIMATION STRATEGIES

In this section, four Doppler estimation strategies are presented, denoted as *point*, *linear*, *midamble-point* and *midamble-linear* estimation.

A. POINT ESTIMATION

The point estimation strategy leverages the last synchronization downchirp in the preamble of the LoRa frame, illustrated in Fig. 6, which is used to estimate the Doppler effect in the subsequent payload.

Similar to the procedure for demodulating an upchirp corresponding to a symbol s_n from the modulation alphabet, as explained in Section III-B, the synchronization downchirp is demodulated by multiplying its complex envelope by the complex envelope of a pure upchirp, whose frequency increases linearly from $-\frac{B}{2}$ to $\frac{B}{2}$. The result of this product, $s_{\text{point}}(t)$, is then subjected to a Fourier transform. The bin S_{point}, where the peak of the Fourier transform appears corresponds to the Doppler shift experienced by the considered synchronization downchirp, so that

$$S_{\text{point}} = \text{argmax}_f \left| \mathcal{F}\{s_{\text{point}}(t)\} \right|, \tag{10}$$

with $\mathcal{F}\{.\}$ denoting the Fourier transform. Clearly, in the absence of any Doppler-induced frequency shift, $S_{\text{point}} = 0$. The estimated Doppler-induced phase shift is then obtained as

$$\hat{\theta}_{\text{point}}(t) = 2\pi\, S_{\text{point}}\, t. \tag{11}$$

Given (11), the complex envelope $i_n(t)$ of the received chirp (5), with n spanning all chirps in the payload, is multiplied by $\exp(-j\,\hat{\theta}_{\text{point}}(t))$ to obtain the Doppler-compensated signal with complex envelope

$$\hat{i}_n(t) = i_n(t) \exp\Big(-j\,\hat{\theta}_{\text{point}}(t)\Big). \tag{12}$$

This operation corrects for the Doppler-induced phase variations across the entire payload, assuming that the Doppler shift remains constant throughout the entire ToA. The compensated signal, as expressed in (12), is then demodulated by performing the dechirping operation (5), followed by the Fourier transform, as described in [12].

Remark 1: This strategy is quite simple and straightforward, representing a simplified version of the solution proposed in [41], which estimates the Doppler shift as the average shift experienced across all upchirps in the preamble. Here, we decided to leverage only the last downchirp in the preamble because it is the closest to the payload, which is the part of the frame that needs to be demodulated with the highest accuracy. Conversely, the averaging operation carried out in [41] makes the estimated Doppler shift dependent also on the upchirps that are farther from the payload, increasing the risk that the estimate does not accurately reflect the Doppler conditions affecting the payload. Nevertheless, neither this approach nor the one in [41] can compensate for the Doppler rate, as the Doppler shift, estimated from the preamble, is considered constant throughout the entire ToA. This approach serves as a baseline in this paper to evaluate the improvements achievable with more sophisticated strategies.

B. LINEAR ESTIMATION

The linear estimation approach takes into account the first and last synchronization downchirps within a LoRa frame, as highlighted in Fig. 7.

Specifically, the estimated Doppler shift at any given time instant t within the frame duration is obtained using a linear model that interpolates between the frequency deviations at the first and last synchronization downchirps. Therefore, the frequency deviation due to the Doppler effect is modeled as

$$\gamma(t) = \alpha(t - T_{\text{start}}) + S_{\text{linear}}[1], \tag{13}$$

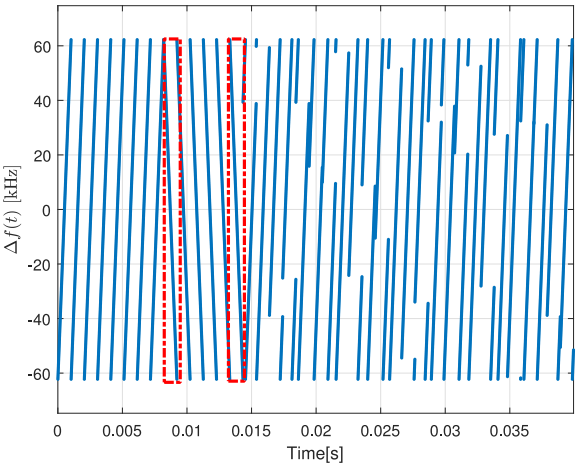

FIGURE 7. Frequency deviation within a LoRa frame with $n_{up} = 8$, $n_{dw} = 6$ and $n_{sym} = 25$. The dotted-dashed red line indicates the two downchirps used for linear Doppler estimation.

where $S_{\text{linear}}[n]$, with $n \in \{1, \ldots, n_{\text{dw}}\}$, denotes the frequency bins in which the spectrum peaks appear for each synchronization downchirp. Here, T_{start} denotes the time instant corresponding to the beginning of the first downchirp, which experiences the estimated Doppler shift $S_{\text{linear}}[1]$.

In light of the above, the angular coefficient α, which quantifies the rate of change of the frequency deviation over time, is computed as

$$\alpha = \frac{S_{\text{linear}}[n_{\text{dw}}] - S_{\text{linear}}[1]}{T_{\text{c}}(n_{\text{dw}} - 1)}, \tag{14}$$

where $S_{\text{linear}}[n_{\text{dw}}]$ and $S_{\text{linear}}[1]$ are obtained using the same procedure described in Section VI-A to derive S_{point}.

This formulation models the variation of the Doppler shift during the reception of the downchirps as linear and assumes that this linear trend persists throughout the entire frame duration, i.e., for the entire ToA. This approach offers a potential improvement over baseline point estimation introduced in Section VI-A, where a single frequency shift is estimated and applied to compensate for the Doppler effect over the entire frame. This is particularly relevant when the Doppler rate is significant, such as when the satellite is at its closest distance to the IoT device.

Given (13), the estimated Doppler-induced phase shift is immediately obtained as follows

$$\hat{\theta}_{\text{linear}}(t) = 2\pi\, t\left[\frac{1}{2}\alpha t - \alpha T_{\text{start}} + S_{\text{linear}}[1]\right]. \tag{15}$$

This estimate is then used to obtain the Doppler-compensated signal

$$\hat{i}_n(t) = i_n(t)\exp\left(-j\,\hat{\theta}_{\text{linear}}(t)\right), \tag{16}$$

which is subsequently demodulated, through dechirping and Fourier transform, following the procedure outlined in [12].

Remark 2: As clearly shown in Fig. 4, the Doppler shift variation during the entire satellite visibility period does not follow a linear trend. At first glance, this appears to contradict the fundamental assumption underlying the strategy introduced in this section—namely, that the Doppler shift varies linearly over time. However, the key requirement for this strategy to be effective is that the Doppler shift remains approximately linear within the ToA of the received frame. Since the ToA depends on various factors, such as the selected SF and payload length, and given that the profile of the Doppler shift within the ToA is influenced by the satellite's orbital position, this aspect requires further investigation, which is addressed in the numerical results section.

It is worth noting, furthermore, that in order to increase the accuracy of α, the two downchirps used for its estimation should be well separated. This would require increasing the number of downchirps in the preamble and, consequently, modifying the frame format compared to the one currently defined, which includes only 2.25 downchirps. Therefore, this approach is not compliant with the current LoRaWAN specification. It is presented here as a potential enhancement for future DtS systems where the frame structure could be optimized for high-Doppler conditions. This is exemplified in Fig. 7, which shows a frame with six downchirps.

C. MIDAMBLE-BASED ESTIMATIONS

In principle, the linear estimation strategy presented in Section VI-B constitutes a refinement of the point estimation approach, as it incorporates some Doppler rate effects. However, its accuracy depends on the assumption that the Doppler shift varies linearly over the frame's ToA. In scenarios where the Doppler shift exhibits non-linear variations over the duration of a frame, as can occur with long frames, this assumption may result in estimation inaccuracies.

To address this limitation, the midamble-point and midamble-linear estimation strategies refine the point and linear estimation approaches, respectively. These strategies leverage pilot upchirps embedded within the payload to iteratively refine the Doppler estimate. These pilots, referred to as midambles, are strategically placed at regular intervals throughout the payload, enabling the receiver to dynamically adapt to Doppler variations. From a practical standpoint, a midamble consists of a pure upchirp, which corresponds to symbol 0 in the modulation alphabet. Therefore, inserting a midamble into the payload at the transmitter side simply involves placing a 0 in the appropriate position within the symbol sequence representing the transmitted data. These additional symbols are, of course, discarded by the receiver when extracting the actual data. Examples of the resulting frames for both strategies are illustrated in Fig. 8 (midamble-point strategy) and Fig. 9 (midamble-linear strategy).

1) MIDAMBLE-POINT ESTIMATION

The midamble-point strategy begins with an initial estimate of the Doppler-induced phase shift, denoted as $\hat{\theta}_{\text{point,mid}}[1]$, computed using the last downchirp of the preamble, similar to (11). This estimate is then iteratively refined as new

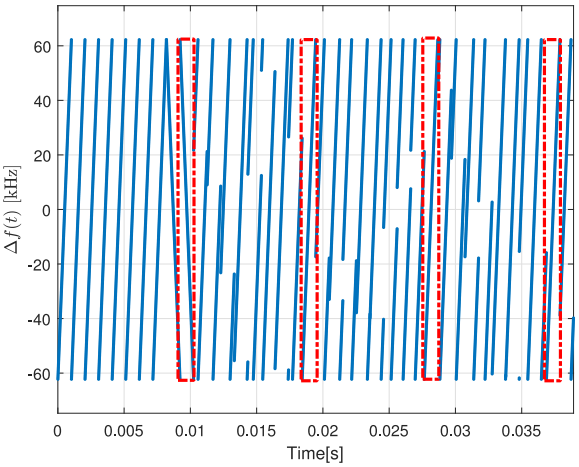

FIGURE 8. Frequency deviation within a LoRa frame with $n_{\text{up}} = 8$, $n_{\text{dw}} = 2$ and $n_{\text{sym}} = 25$. The dotted-dashed red lines indicate the preamble downchirp and the midamble upchirps used for midamble-point Doppler estimation updates.

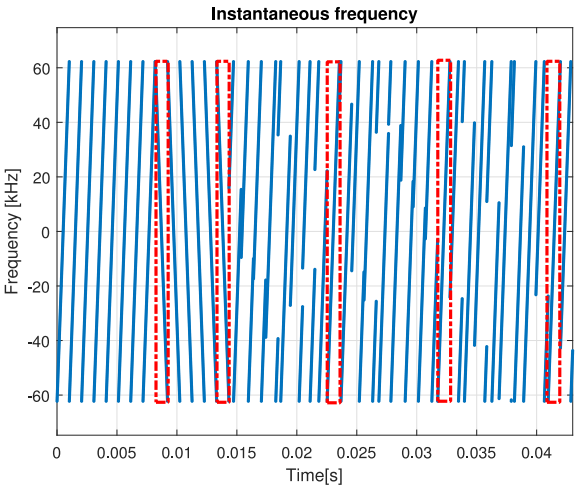

FIGURE 9. Frequency deviation within a LoRa frame with $n_{\text{up}} = 8$, $n_{\text{dw}} = 6$ and $n_{\text{sym}} = 25$. The dotted-dashed red lines indicate the preamble downchirp and the midamble upchirps used for midamble-linear Doppler estimation updates.

midambles are received. Specifically, the Doppler-induced phase shift at the m-th midamble update step, where $m \in \{2, \ldots, n_{\text{point,mid}}\}$ and $n_{\text{point,mid}}$ is the total number of midambles, is given by

$$\hat{\theta}_{\text{point,mid}}[m] = \hat{\theta}_{\text{point,mid}}[m-1] + \Delta\hat{\theta}_{\text{point,mid}}[m], \quad (17)$$

where $\Delta\hat{\theta}_{\text{point,mid}}[m]$ is the correction term derived from the frequency offset estimated using the m-th midamble. This correction term is computed using the same procedure described in Section VI-A for point estimation, where the peak of the Fourier transform of the dechirped midamble signal corresponds to the Doppler shift.[9]

[9]Note that the proposed design iteratively refines the Doppler shift estimate using upchirps in the midambles (within the payload), in contrast to the initial estimate derived from downchirps in the preamble.

The Doppler-compensated signal for the n-th chirp in the payload is then obtained by applying the updated phase shift estimate

$$\hat{i}_n(t) = i_n(t) \exp\Big(-j\,\hat{\theta}_{\text{point,mid}}(t)\Big). \quad (18)$$

Remark 3: According to this strategy, the Doppler shift is modeled as a piecewise constant function. The effectiveness of this approach hinges on the midamble update interval, $T_{\text{point,mid}}$, which must be carefully selected to ensure that Doppler-induced frequency errors are corrected before they lead to symbol demodulation failures. This interval is governed by two competing factors: the rate of frequency error accumulation, ξ, which is driven by the Doppler rate, and the system's resilience to such errors. The system's resilience is proportional to the frequency separation between adjacent LoRa symbols, given by $\frac{B}{2^{\text{SF}}}$.

A key aspect of LoRa modulation is that its symbol rate, R_{s}, is equivalent to this frequency separation, $R_{\text{s}} = \frac{B}{2^{\text{SF}}}$. This equivalence directly links a higher symbol rate to increased robustness against frequency deviations. Consequently, the maximum update interval, $T_{\text{point,mid}}$, can be defined as the time during which the accumulated frequency shift, $|\xi| \cdot T_{\text{point,mid}}$, remains below a tolerable threshold, $k \cdot R_{\text{s}}$, where k is a system tolerance factor.[10] This leads to the following relationship:

$$T_{\text{point,mid}} = \frac{k}{|\xi|} \cdot R_{\text{s}}. \quad (19)$$

This relationship reveals a direct proportionality between the update interval $T_{\text{point,mid}}$ and the symbol rate R_s. The physical reasoning is that a higher symbol rate (achieved with a lower SF) inherently provides greater frequency separation between symbols. This enhanced separation makes the system more tolerant to frequency shifts, thus allowing for a longer time to elapse before compensation becomes necessary for a given ξ. Then, the optimal number of midambles $n^{\star}_{\text{point,mid}}$ is given by

$$n^{\star}_{\text{point,mid}} = \left\lceil \frac{T_{\text{c}}\, n_{\text{sym}}}{T_{\text{point,mid}}} \right\rceil = \left\lceil \frac{n_{\text{sym}}}{n_{\text{int, point}}} \right\rceil, \quad (20)$$

where $n_{\text{int,point}}$ is the number of chirps between consecutive midambles for midamble-point strategy. For instance, consider $B = 125$ kHz, SF $= 10$, $k = 0.1$, $n_{\text{sym}} = 15$, $T_{\text{c}} = 8.2 \cdot 10^{-3}$ s and $\xi = -304.71$ Hz/s. Substituting these values into (19) yields $T_{\text{point,mid}} = 0.0401$ s. Applying this result to (20) yields $n^{\star}_{\text{point,mid}} = 4$ midambles.

However, in practice, determining the exact number of midambles required for Doppler compensation on a per-frame basis is impractical, as ξ depends on the relative position between the satellite and the terrestrial device at

[10]Following [48], a frequency shift caused by the Doppler effect results in a mismatch Δf between the LoRa receiver's frequency settings and the incoming signal. If the receiver is perfectly time-aligned with the LoRa symbol and $|\Delta f| > 0.5\,B/M$, a symbol error occurs. Even when this condition is not met, noise may still cause symbol errors. Therefore, we consider typical values of k ranging from 0 to 0.5.

the time of transmission. Accurately estimating this would require the transmitter to know both its own position and that of the receiver. In the uplink, this would necessitate equipping terrestrial devices with positioning capabilities (e.g., GNSS) and access to satellite ephemerides, while in the downlink, the satellite would need precise knowledge of the receiver's coordinates. Moreover, a computational effort is required for each transmission. A more practical approach is to adopt a fixed-interval midamble insertion strategy, where the number and placement of midambles are predetermined based on the system design and expected worst-case operating conditions. While this method simplifies implementation, it may lead to suboptimal performance when the Doppler shift varies significantly over the frame duration. The trade-offs associated with the number of midambles are further explored in the numerical results section.

2) MIDAMBLE-LINEAR ESTIMATION

The midamble-linear strategy extends the basic linear estimation approach described in Section VI-B by dynamically refining the Doppler shift estimate using midambles that are distributed throughout the frame and spaced every $n_{\text{int,linear}}$ chirps. Unlike the static linear model, this method iteratively updates both the Doppler shift and its rate of change, allowing for tracking of time-varying Doppler effects within the payload as well.

The process begins with an initial estimate of the Doppler-induced phase shift, obtained from the preamble downchirps using the procedure outlined in Section VI-B. This provides a baseline Doppler shift $S_{\text{linear,mid}}[1]$ and rate $\alpha_{\text{mid}}[1]$, where $m = 1$ refers to the initial estimates obtained from the preamble downchirps.

For each subsequent midamble $m \in \{2, \ldots, n_{\text{linear,mid}}\}$ in the payload, with $n_{\text{linear,mid}}$ denoting the total number of midambles, the Doppler shift $S_{\text{linear,mid}}[m]$ is estimated by locating the peak of the Fourier transform of the dechirped midamble signal, following the same procedure as in Section VI-A. The updated Doppler rate $\alpha_{\text{mid}}[m]$ is then computed as the slope between the current and previous midamble, given by

$$\alpha_{\text{mid}}[m] = \frac{S_{\text{linear,mid}}[m] - S_{\text{linear,mid}}[m-1]}{T_m - T_{m-1}}, \tag{21}$$

where T_m and T_{m-1} denote the time instants of the m-th and $(m-1)$-th midambles, respectively. This refined rate is used to adjust the phase shift estimate for the next segment, expressed as

$$\hat{\theta}_{\text{linear,mid}}(t) = 2\pi t \Big[\frac{1}{2}\alpha_{\text{mid}}[m]t - \alpha_{\text{mid}}[m]T_{m-1} + S_{\text{linear,mid}}[m-1] \Big]. \tag{22}$$

The compensated signal for each payload chirp is then obtained by applying the corresponding phase correction

$$\hat{i}_n(t) = i_n(t) \exp\Big(-j\hat{\theta}_{\text{linear,mid}}(t)\Big). \tag{23}$$

Remark 4: According to this strategy, the Doppler shift is modeled as a piecewise linear function, allowing for varying slopes in the intervals between midambles. This approach potentially provides superior tracking of Doppler variations compared to the basic linear estimation, particularly for longer frames where non-linear effects become significant. The trade-off between estimation accuracy and additional midambles introduced will be quantitatively analyzed in the numerical results section.

VII. NUMERICAL RESULTS

This section presents numerical results evaluating the performance of the proposed Doppler estimation and compensation strategies. The assessment was conducted using an extended version of the validated LoRa physical-layer simulator [12], modeling a satellite communication link. The simulated link comprises a LoRa transmitter, a propagation channel characterized by Rician fading, with Rician factor $K = 10$ dB [49], additive white Gaussian noise (AWGN), and Doppler effect, and a receiver. Concerning the propagation channel, we adopted the generalized model for a LEO satellite in a circular orbit as derived in [50]. This model provides a robust analytical function for the Doppler shift. While this manuscript focuses on higher-level algorithmic performance, the underlying physical model has been subject to rigorous real-world validation. Specifically, the work in [51] utilized this exact modeling approach to pre-compensate for Doppler shift in direct-to-satellite LoRa transmissions. The results therein show a strong agreement between the Doppler curve predicted by the model and orbital measurement data collected from the TIANQI-7 satellite.

A. SCENARIOS, PARAMETERS AND PERFORMANCE METRIC

Various scenarios were considered, accounting for different satellite positions and multiple LoRa configurations, as detailed in Table 2. Specifically, we analyzed the uplink of a DtS LoRa link established by an IoT terrestrial device communicating with a LEO satellite at an altitude of 550 km. At the maximum elevation angle, the satellite was assumed to be directly overhead of the IoT device. Two satellite positions along the orbit, as illustrated in Fig. 5, were examined: *Case 1*, characterized by a high Doppler shift and a low Doppler rate (corresponding to a low elevation angle), and *Case 2*, exhibiting the opposite conditions (corresponding to a high elevation angle).

Regarding the LoRa signal, we considered a bandwidth of $B = 125$ kHz, centered at a carrier frequency of $F_C = 868$ MHz, with spreading factors SF = 7 and SF = 12. Additionally, we investigated the impact of the LDRO mode, which enhances robustness against Doppler effects.

For the frame format, the preamble consisted of $n_{\text{up}} = 8$ upchirps, followed by $n_{\text{dw}} = 2$ downchirps for the point-based estimation strategies, or $n_{\text{dw}} = 6$ downchirps for the linear-based estimation strategies. The choice of $n_{\text{dw}} = 2$ for the point-based strategies is based on the standard LoRa

frame structure, which includes two complete downchirps. For the linear-based estimation strategies, $n_{\mathrm{dw}} = 6$ is chosen to improve the estimation of the angular coefficient α, which represents the rate of change of the frequency deviation over time, by utilizing a larger number of downchirps in the preamble. We acknowledge that using $n_{\mathrm{dw}} = 6$ downchirps introduces a ToA overhead not present in standard frames. While the present study is focused on symbol error rate (SER) as a primary metric for physical layer robustness against Doppler effects, the resulting trade-off between SER performance and spectral efficiency is a key factor for practical throughput that merits future analysis.

Additionally, unless stated otherwise, the payload size was set to $L = 120$ bits. In all cases, we assumed that the parameter CR, which denotes the coding rate according to LoRa specification, is set to 1, meaning that one parity bit is added for every four data bits. For the midamble-based strategies, the interval $n_{\mathrm{int,point}}$ between consecutive midambles in the midamble-point approach is set to three chirps at SF $=$ 12 and twelve chirps for SF $=$ 7. In the midamble-linear strategy, the interval $n_{\mathrm{int,linear}}$ is set to 6 chirps for all configurations.

For each scenario and parameter setting, the performance of the estimation strategies was evaluated in terms of SER, which also corresponds to the chirp error rate. In addition, we define the SNR, as $\mathrm{SNR} = \frac{P}{P_{\mathrm{n}}}$, where P represents the average received signal power and P_{n} the noise power within the bandwidth B. Finally, for comparison, performance was also assessed in a benchmark scenario with Rician fading and AWGN but without Doppler effects.[11]

B. INFLUENCE OF SNR AND SATELLITE POSITION

Initially, Fig. 10 presents the SER as a function of the SNR for different spreading factors, SF $\in \{7, 12\}$, in the *Case 1* scenario, where high Doppler shift and low Doppler rate conditions are considered. For benchmarking, a comparison with the approach proposed in [40] is also included. As observed, both point and midamble-point estimation techniques yield satisfactory results in terms of error rate performance. Interestingly, the linear-based estimation approaches demonstrate inferior performance. This is because, despite the presence of a high overall Doppler shift, the rate of change of this shift within the short duration of a single LoRa frame is minimal. In such conditions, attempting to impose a linear estimation across the frame can inadvertently amplify the effects of noise and the finite resolution of the FFT on the Doppler shift estimate, as the actual frequency variation is very close to constant. Consequently, the point estimation, relying on a single robust measurement, proves more accurate and less susceptible to noise compared to the calculation of a slope over such a limited time window where the change is negligible. It is worth noting, however, that the midamble-linear approach mitigates this issue to some extent, offering improved performance compared to the standard linear estimation under these specific conditions. Finally, while the benchmark approach from [40] achieves near-optimal performance for SF $=$ 7, this comes at the cost of significantly higher computational complexity. In fact, the approach therein relies on an iterative, decision-directed loop that stores and refines estimates over multiple symbols. Our proposed non-iterative strategies, particularly the point-based methods in this low-rate scenario, offer a compelling trade-off, achieving comparable performance with a much simpler, open-loop implementation that is better suited for resource-constrained IoT receivers. Furthermore, for SF $= 12$, the method in [40] exhibits performance loss, as iterative estimation of channel impairments impedes accurate estimation during large ToA transmissions.

Next, we examine *Case 2*, which considers a scenario with a low Doppler shift but a high Doppler rate. The corresponding SER is illustrated in Fig. 11. In this case, the performance of the point estimation method deteriorates as the spreading factor increases. This degradation is attributed to the increased ToA, which reduces the precision of the estimation process for higher SF values, which exposes the limitation of the point estimation's assumption of a constant Doppler shift throughout the frame. This effect is particularly noticeable for SF $=$ 12, where the linear estimation method outperforms the point estimation technique. In this specific high Doppler rate, long-time-on-air regime, the linear estimation, by considering the Doppler shift at two different points in time, effectively captures

TABLE 2. Scenarios and parameter settings.

Orbital Height	550 km
Satellite Position	*Case 1*, *Case 2*
Bandwidth	125 kHz
Carrier Frequency (F_{C})	868 MHz
Spreading Factors (SFs)	7, 12
LDRO	On, Off
n_{up}	8
n_{dw}	2, 6
$n_{\mathrm{int,point}}$	SF $= 12:$ 3, SF $= 7:$ 12
$n_{\mathrm{int,linear}}$	6
Payload Size	120 bits
Coding Rate (CR)	1

[11] While ionospheric scintillation is a significant impairment in satellite communications, its accurate modeling and compensation, particularly regarding the complex requirements for robust carrier synchronization, extend beyond the scope of this work. We defer its detailed investigation to future research.

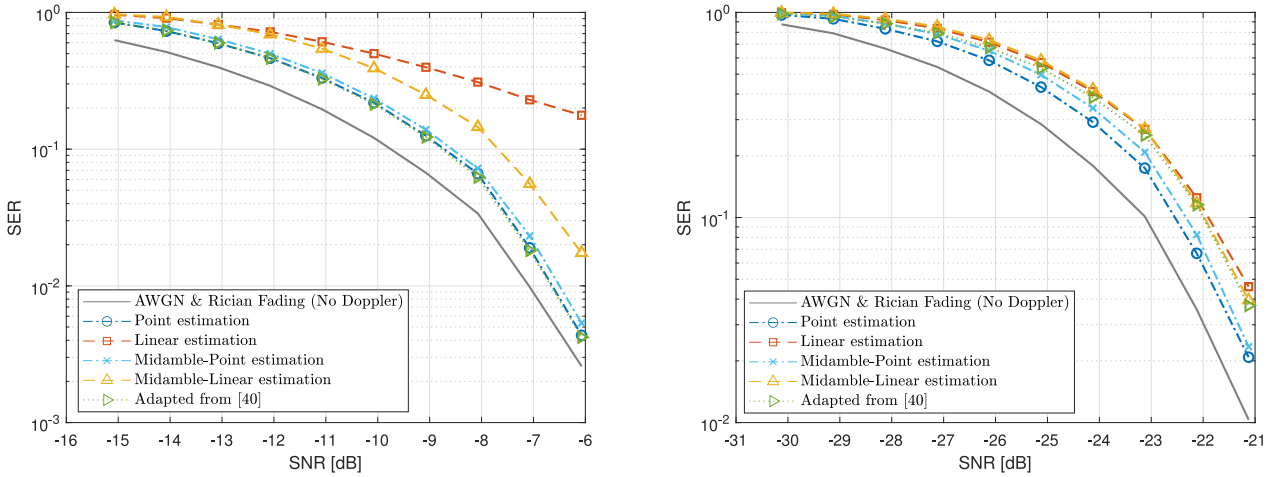

FIGURE 10. Symbol error rate (SER) performance of the proposed Doppler estimation and compensation framework in comparison with the framework of [40] across different spreading factors in *Case 1*. From left to right: results for SF = 7 and SF = 12.

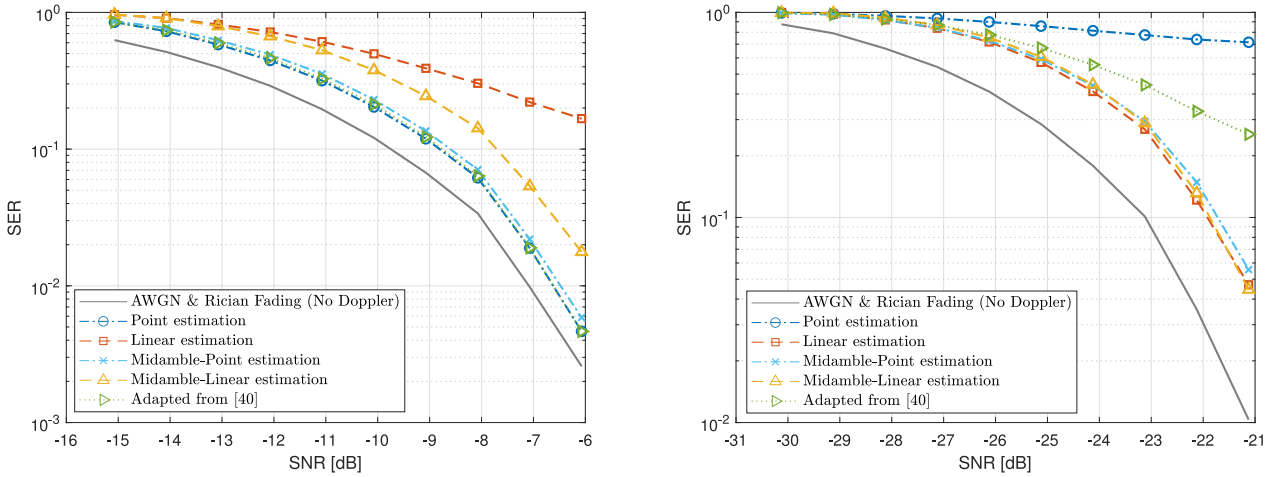

FIGURE 11. Symbol error rate (SER) performance of the proposed Doppler estimation and compensation framework in comparison with the framework of [40] across different spreading factors in *Case 2*. From left to right: results for SF = 7 and SF = 12.

the linear component of the rapid Doppler rate. While not a perfect representation of the underlying non-linear (exponential) change, this linear approximation provides a much better fit than the static model of the point estimation under these challenging conditions, thus resulting in a lower error rate. In this regard, we observe that the method of [40] provides an inferior performance for SF = 12 combined with higher Doppler rate. This scenario particularly challenges the symbol refining strategy proposed in [40], where the iterative estimation over channel impairments like AWGN and Rician fading hinders a correct estimation of the rapidly changing Doppler rate, directly impacting the SER. Furthermore, for both *Case 1* and *Case 2*, we observe that the midamble-point-based approaches consistently deliver performance close to the best technique in each scenario. This highlights its versatility as a practical design choice.

To further refine the previous analysis, Fig. 12 presents the SER performance of various estimation strategies at a fixed $E_s/N_0 = 15$ dB. Here, E_s denotes the average energy of the received chirp, while N_0 represents the single-sided noise power spectral density. The parameter E_s/N_0 characterizes the ratio of the average symbol energy to noise power spectral density, which is related to the SNR through the expression[12] $\text{SNR} = \frac{E_s}{N_0}\frac{1}{2^{\text{SF}}}$, which corresponds to an SNR of -6.07 dB for SF $= 7$ and -21.12 dB for SF $= 12$. The analysis considers intermediate satellite positions between *Case 1* and *Case 2*, as illustrated in Fig. 4. Specifically, simulations were conducted at time instances $t \in \{-366\text{s}, -274.5\text{s}, -183\text{s}, -91.5\text{s}, 0\text{s}\}$, corresponding to distinct Doppler realizations that progressively transition between the two extreme cases analyzed previously. For conciseness, we focus on SF $= 7$ and SF $= 12$, representing the two boundary conditions in terms of spreading factor. The results highlight that the midamble-point estimation

[12] From $\text{SNR} = \frac{P}{P_n}$, it follows that $\text{SNR} = \frac{P}{P_n} = \frac{E_s/T_c}{N_0 B} = \frac{E_s}{N_0}\frac{1}{BT_c}$. Given the relationship $BT_c = 2^{\text{SF}}$, which holds for the LoRa modulation, we finally obtain $\text{SNR} = \frac{P}{P_n} = \frac{E_s}{N_0}\frac{1}{2^{\text{SF}}}$.

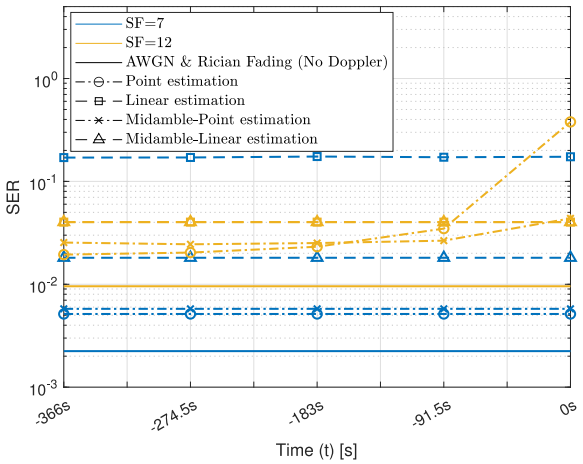

FIGURE 12. SER performance of different estimation strategies at a fixed $E_s/N_0 = 15$ dB, which corresponds to an SNR of -6.07 dB for SF $= 7$ and -21.12 dB for SF $= 12$. Intermediate satellite positions between *Case 1* and *Case 2* are considered.

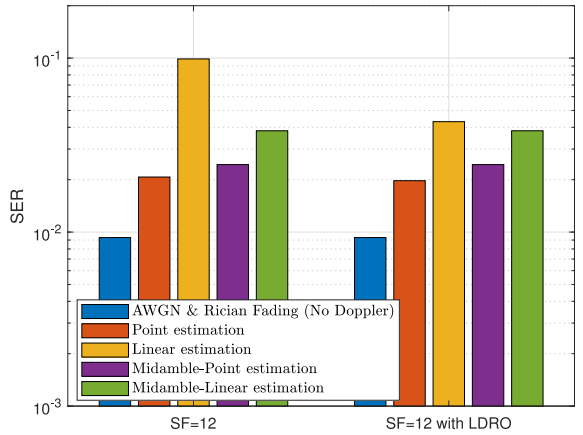

FIGURE 13. SER performance for SF $= 12$ with and without LDRO, considering fixed SNR $= -21.12$ dB and $L = 120$ bits in the *Case 1* scenario.

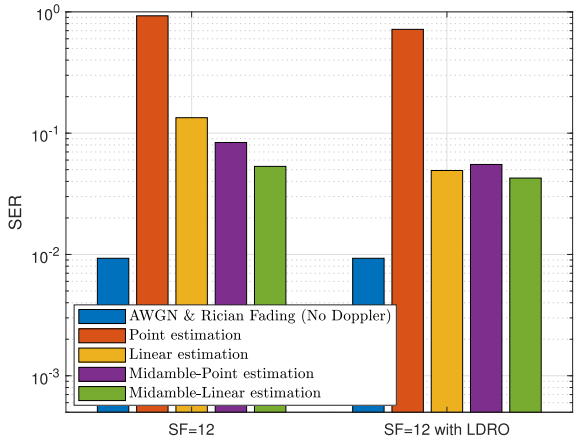

FIGURE 14. SER performance for SF $= 12$ with and without LDRO, considering fixed SNR $= -21.12$ dB and $L = 120$ bits in the *Case 2* scenario.

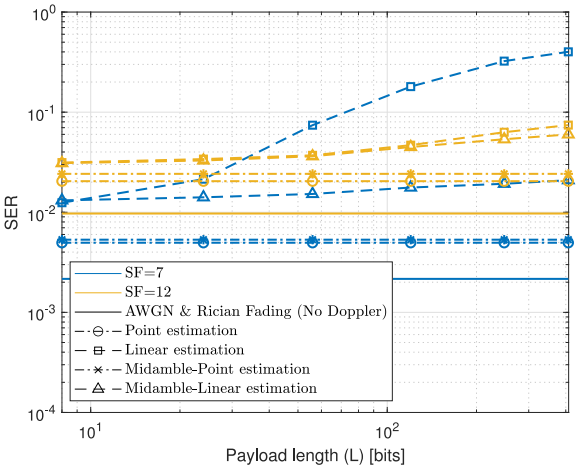

FIGURE 15. SER performance as a function of payload length for a fixed $E_s/N_0 = 15$ dB, which corresponds to an SNR of -6.07 dB for SF $= 7$ and -21.12 dB for SF $= 12$, in the *Case 1* scenario.

consistently achieves performance close to the optimal strategy across all intermediate satellite positions, reinforcing its robustness under varying Doppler conditions. Furthermore, the analysis reveals critical transition points, at specific values of t, where the performance of the point-based and linear-based estimation techniques intersect, indicating shifts in their relative effectiveness due to the dynamic Doppler characteristics.

Finally, Fig. 13 and Fig. 14 present a comparative analysis of the SER performance for SF $=$ 12, evaluating the impact of enabling the LDRO mode. The results are obtained under fixed conditions of $E_s/N_0 =$ 15 dB and a payload length of $L = 120$ bits, allowing for a direct assessment of the performance gains achieved through this optimization. Fig. 13 illustrates the results for *Case 1*, while Fig. 14 depicts the performance for *Case 2*. The findings highlight that enabling LDRO improves robustness against Doppler-induced distortions, particularly for *Case 2*, with higher frequency variations.

C. INFLUENCE OF THE PAYLOAD LENGTH

The influence of payload length on each estimation framework is illustrated in Fig. 15 and Fig. 16 for *Case 1* and *Case 2*, respectively. Considering the LoRaWAN maximum application payload length for the EU863-870 regional parameters, the maximum payload length is 51 bytes for SF $=$ 12, and 222 bytes for SF $=$ 7, all operating at a bandwidth of 125 kHz. Therefore, for comparison purposes, we consider a maximum payload size of 51 bytes for all curves, and we set $E_s/N_0 =$ 15 dB. Interestingly, Fig. 15 demonstrates that in scenarios with high Doppler shift and low Doppler rate, the impact of payload length is limited to the linear-based estimation frameworks. In this case, the point and midamble-point estimation frameworks perform robustly across Doppler realizations, maintaining high accuracy despite variations in payload length.

However, such stable behavior of the point estimation does not hold when the payload length increases in *Case 2*. In this scenario, due to the high Doppler rate, the estimations provided by both the point and linear estimation

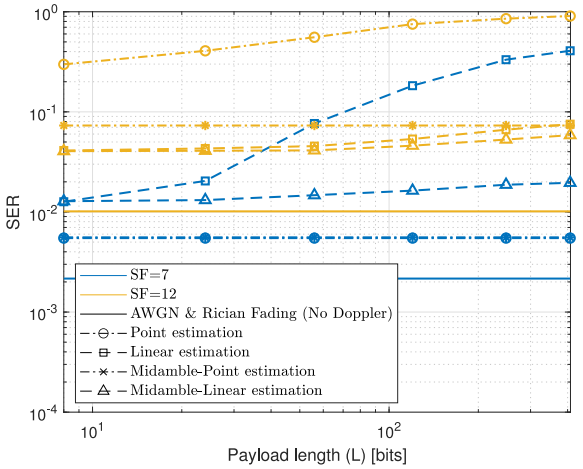

FIGURE 16. SER performance as a function of payload length for a fixed $E_s/N_0 = 15$ dB, which corresponds to an SNR of -6.07 dB for SF $= 7$ and -21.12 dB for SF $= 12$, in the *Case 2* scenario.

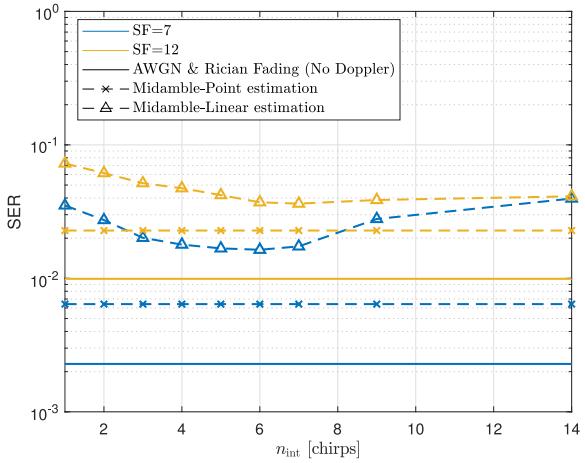

FIGURE 17. SER as a function of n_{int} for point and linear midamble estimation frameworks in *Case 1* scenario.

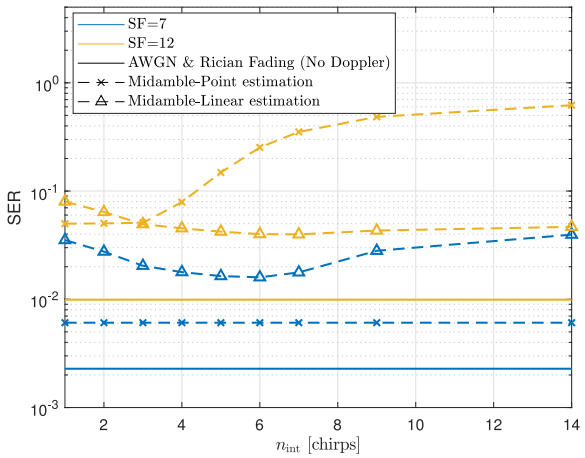

FIGURE 18. SER as a function of n_{int} for point and linear midamble estimation frameworks in *Case 2* scenario.

frameworks become increasingly inaccurate as the frame's ToA increases. This results in a significant rise in the SER as L increases. In contrast, the midamble-point strategy, which uses midamble pilot downchirps embedded within the payload to continuously refine the Doppler estimate, offers consistent performance even with longer payloads.

D. IMPACT OF MIDAMBLE SPACING

In Section VI-C, we introduced the parameters $n_{\text{int,point}}$ and $n_{\text{int,linear}}$, which denote the number of chirps between consecutive midambles in the midamble-point and midamble-linear strategies, respectively. To evaluate their impact, this section analyzes the SER across different spreading factors, considering various midamble spacings. For conciseness, both $n_{\text{int,point}}$ and $n_{\text{int,linear}}$ are hereafter denoted by the compact notation n_{int}.

For this analysis, we also set $E_s/N_0 = 15$ dB. In this regard, Fig. 17 and Fig. 18 demonstrate how increasing n_{int} affects estimation accuracy and, consequently, the resulting SER for *Case 1* and *Case 2*, respectively, in both frameworks.

Specifically, Fig. 17 demonstrates that higher values of n_{int}, corresponding to longer intervals between estimations, are sufficient to achieve optimal midamble-point estimation in scenarios with high Doppler shifts but low Doppler rates. This observation aligns with prior analyses, as the Doppler effects are often adequately captured by the last downchirp in the preamble of a LoRa frame, requiring no further refinement. Conversely, Fig. 18 reveals that selecting an appropriate n_{int} becomes critical in scenarios with both high SF and high Doppler rates. Here, refining Doppler estimation via the midamble-point strategy yields significant SER improvements. These findings are consistent with the n_{int} values listed in Table 2. Regarding the midamble-linear estimation, we observe that lower n_{int} values introduce inaccuracies in the linear estimation. This occurs because closely spaced midamble chirps, analogous to the linear strategy, compromise the precision of α_{mid}. To enhance accuracy, the midambles used for estimation should be sufficiently separated.

E. PRACTICAL ASPECTS

To evaluate the practical implications of the proposed frameworks, we assess the additional latency and energy consumption introduced by each Doppler estimation strategy. We analyze the ToA overhead from extra preamble downchirps and payload midambles. It's important to note that ToA is inversely proportional to bandwidth; a wider bandwidth enables a faster chip rate, which in turn reduces the time required to transmit symbols and thus the overall packet. Therefore, we quantify the impact of this increased ToA on energy consumption by estimating the reduction in battery lifetime for a typical IoT device. For this analysis, we consider an end device with a 230 mAh battery transmitting a 15-byte packet every 900 seconds, using the LoRa energy consumption model from [51].

Table 3 reports the ToA for each framework, considering SF $\in \{7, 12\}$ and the number of chirps between consecutives

TABLE 3. ToA of the proposed doppler estimation strategies.

Strategy	ToA [s]	
	$\mathbf{SF = 7}$	$\mathbf{SF = 12}$
Point Estimation	0.044	1.090
Linear Estimation	0.048	1.221
Midamble-Point Estimation	0.047	1.341
Midamble-Linear Estimation	0.054	1.346

TABLE 4. Impact on battery lifetime of the proposed doppler estimation strategies.

Strategy	Battery Lifetime [years]	
	$\mathbf{SF = 7}$	$\mathbf{SF = 12}$
Point Estimation	10.115	0.645
Linear Estimation	9.590	0.579
Midamble-Point Estimation	9.716	0.529
Midamble-Linear Estimation	8.896	0.527

midambles n_{int}, either $n_{\text{int,point}}$ or $n_{\text{int,linear}}$, configured as specified in Table 2. As expected, the point estimation strategy introduces no ToA overhead compared to the legacy LoRa frame, as it leverages the legacy LoRa frame's existing preamble structure. We've therefore omitted the legacy LoRa frame from Table 3 for brevity. In contrast, the linear estimation strategy adds a small, fixed overhead from the four extra downchirps. The midamble-based strategies introduce a variable overhead that is most pronounced for the midamble-linear strategy at SF = 12. In this case, the frequency of midamble insertions causes a ToA increase of over 23.5%, a necessary trade-off for reducing the SER under challenging Doppler conditions.

This increased ToA directly translates to higher energy consumption per transmission, which in turn reduces the operational lifetime of battery-powered devices. Table 4 quantifies this impact across different SF scenarios. For instance, the ToA of the midamble-point strategy at SF = 12 reduces the battery lifetime by approximately 18% compared to the point estimation.

The reduction in power efficiency is a justifiable trade-off for the significant gains in communication robustness achieved under high-Doppler rate conditions. Given the paramount importance of link reliability, the midamble approach presents a practical and advantageous solution where the marginal increase in power expenditure is warranted by the substantial performance improvement.

VIII. CONCLUSION

This paper investigates the impact of the Doppler effect on LoRa-based DtS communication in LEO satellite scenarios. In this context, we analyzed both Doppler shift and Doppler rate, proposing and evaluating four distinct Doppler estimation and compensation frameworks: point, linear, midamble-point and midamble-linear estimation. Through comprehensive numerical simulations aligned with LoRaWAN specifications, including the LDRO feature, we assess the effectiveness of these frameworks in mitigating Doppler-induced distortions and ensuring reliable communication. Our results highlight the critical importance of selecting appropriate estimation strategies based on specific LoRa parameters, such as the spreading factor and the interplay between Doppler shift and signal configuration. Among the proposed methods, point-midamble estimation emerges as the most consistent approach, achieving near-optimal accuracy in the vast majority of scenarios by iteratively refining Doppler shift estimates through midamble symbol integration in LoRa frames. In contrast, point and linear estimation offer simpler, lower-complexity alternatives but suffer from reduced accuracy in dynamic Doppler scenarios. Linear-midamble estimation improves upon linear estimation, yet it still underperforms relative to point-midamble estimation in most scenarios.

REFERENCES

[1] C. Milarokostas, D. Tsolkas, N. Passas, and L. Merakos, "A comprehensive study on LPWANs with a focus on the potential of LoRa/LoRaWAN systems," *IEEE Commun. Surveys Tuts.*, vol. 25, no. 1, pp. 825–867, 1st Quart., 2023.

[2] A. N. Arun, A. B. Das, C. G. Brinton, D. J. Love, and J. V. Krogmeier, "Do small cells make sense for simple low cost LPWANs?" *IEEE Wireless Commun. Lett.*, vol. 13, no. 9, pp. 2352–2356, Sep. 2024.

[3] Y. Guo, J. Niu, X. Zhou, T. Gu, Y. Li, and D. Fang, "Power-efficient transmissions in LoRa uplink systems," *IEEE Trans. Veh. Technol.*, vol. 73, no. 8, pp. 11224–11236, Aug. 2024.

[4] "Key drivers and research challenges for 6G ubiquitous wireless intelligence," 6G Flagship, Univ. Oulu, Oulu, Finland, Rep. 6G Research Visions 1, Sep. 2019.

[5] M. Jouhari, N. Saeed, M.-S. Alouini, and E. M. Amhoud, "A survey on scalable LoRaWAN for massive IoT: Recent advances, potentials, and challenges," *IEEE Commun. Surveys Tuts.*, vol. 25, no. 3, pp. 1841–1876, 3rd Quart., 2023.

[6] Z. Qin, F. Y. Li, G. Y. Li, J. A. McCann, and Q. Ni, "Low-power wide-area networks for sustainable IoT," *IEEE Wireless Commun.*, vol. 26, no. 3, pp. 140–145, Jun. 2019.

[7] H. Jiang, D. Qu, J. Ding, Z. Wang, H. He, and H. Chen, "Enabling LPWAN massive access: Grant-free random access with massive MIMO," *IEEE Wireless Commun.*, vol. 29, no. 4, pp. 72–77, Aug. 2022.

[8] J. A. Fraire, O. Iova, and F. Valois, "Space-terrestrial integrated Internet of Things: Challenges and opportunities," *IEEE Commun. Mag.*, vol. 60, no. 12, pp. 64–70, Dec. 2022.

[9] A. W. Azim, R. Shubair, and M. Chafii, "Chirp spread spectrum-based waveform design and detection mechanisms for LPWAN-based IoT: A survey," *IEEE Access*, vol. 12, pp. 24949–25017, 2024.

[10] J. P. Shanmuga Sundaram, W. Du, and Z. Zhao, "A survey on LoRa networking: Research problems, current solutions, and open issues," *IEEE Commun. Surveys Tuts.*, vol. 22, no. 1, pp. 371–388, 1st Quart., 2020.

[11] O. B. A. Seller, "Wireless communication method," U.S. Patent 9 647 718, 2017. [Online]. Available: http://www.google.it/patents/US9647718

[12] G. Pasolini, "On the LoRa chirp spread spectrum modulation: Signal properties and their impact on transmitter and receiver architectures," *IEEE Trans. Wireless Commun.*, vol. 21, no. 1, pp. 357–369, Jan. 2022.

[13] A. A. Doroshkin, A. M. Zadorozhny, O. N. Kus, V. Y. Prokopyev, and Y. M. Prokopyev, "Experimental study of LoRa modulation immunity to doppler effect in CubeSat radio communications," *IEEE Access*, vol. 7, pp. 75721–75731, 2019.
[14] I. Leyva-Mayorga et al., "LEO small-satellite constellations for 5G and beyond-5G communications," *IEEE Access*, vol. 8, pp. 184955–184964, 2020.
[15] J. A. A. Fraire, S. Céspedes, and N. Accettura, "Direct-to-satellite IoT—A survey of the state of the art and future research perspectives," in *Proc. 18th Int. Conf. Ad-Hoc, Mobile, Wireless Netw.*, 2019, pp. 241–258.
[16] M. A. Ullah, K. Mikhaylov, and H. Alves, "Enabling mMTC in remote areas: LoRaWAN and LEO satellite integration for offshore wind farm monitoring," *IEEE Trans. Ind. Informat.*, vol. 18, no. 6, pp. 3744–3753, Jun. 2022.
[17] M. Asad Ullah, G. Pasolini, K. Mikhaylov, and H. Alves, "Understanding the limits of LoRa direct-to-satellite: The doppler perspectives," *IEEE Open J. Commun. Soc.*, vol. 5, pp. 51–63, 2024.
[18] O. Kodheli et al., "Satellite communications in the new space era: A survey and future challenges," *IEEE Commun. Surveys Tuts.*, vol. 23, no. 1, pp. 70–109, 1st Quart., 2021.
[19] M. Centenaro, C. E. Costa, F. Granelli, C. Sacchi, and L. Vangelista, "A survey on technologies, standards and open challenges in satellite IoT," *IEEE Commun. Surveys Tuts.*, vol. 23, no. 3, pp. 1693–1720, 3rd Quart., 2021.
[20] G. Álvarez, J. A. Fraire, K. A. Hassan, S. Céspedes, and D. Pesch, "Uplink transmission policies for LoRa-based direct-to-satellite IoT," *IEEE Access*, vol. 10, pp. 72687–72701, 2022.
[21] T. T. Nguyen, H. H. Nguyen, R. Barton, and P. Grossetete, "Efficient design of chirp spread spectrum modulation for low-power wide-area networks," *IEEE Internet Things J.*, vol. 6, no. 6, pp. 9503–9515, Dec. 2019.
[22] A. Maleki, H. H. Nguyen, E. Bedeer, and R. Barton, "A tutorial on chirp spread spectrum modulation for LoRaWAN: Basics and key advances," *IEEE Open J. Commun. Soc.*, vol. 5, pp. 4578–4612, 2024.
[23] L. Fernandez, J. A. Ruiz-De-Azua, A. Calveras, and A. Camps, "Assessing LoRa for satellite-to-earth communications considering the impact of ionospheric scintillation," *IEEE Access*, vol. 8, pp. 165570–165582, 2020.
[24] R. Zhang, J. Ma, S. Zhang, and O. A. Dobre, "Fractional chirp rate based CSS division multiple access over LEO satellite Internet-of-Things," *IEEE J. Sel. Topics Signal Process.*, vol. 18, no. 7, pp. 1281–1296, Oct. 2024.
[25] S. Herrería-Alonso, M. Rodríguez-Pérez, R. F. Rodríguez-Rubio, and F. Pérez-Fontán, "Improving uplink scalability of LoRa-based direct-to-satellite IoT networks," *IEEE Internet Things J.*, vol. 11, no. 7, pp. 12526–12535, Apr. 2024.
[26] W. Wu and W. Wang, "Preamble structure and timing advance method for satellite IoT," *IEEE Wireless Commun. Lett.*, vol. 13, no. 4, pp. 1088–1092, Apr. 2024.
[27] E. Testi and E. Paolini, "Packet collision probability of direct-to-satellite IoT systems," *IEEE Internet Things J.*, vol. 12, no. 2, pp. 1843–1855, Jan. 2025.
[28] M. Chiani and A. Elzanaty, "On the LoRa modulation for IoT: Waveform properties and spectral analysis," *IEEE Internet Things J.*, vol. 6, no. 5, pp. 8463–8470, Oct. 2019.
[29] Y. He, Y. Xiao, S. Zhang, M. Jia, and Z. Li, "Direct-to-smartphone for 6G NTN: Technical routes, challenges, and key technologies," *IEEE Netw.*, vol. 38, no. 4, pp. 128–135, Jul. 2024.
[30] L. Zhi et al., "Self-powered absorptive reconfigurable intelligent surfaces for securing satellite-terrestrial integrated networks," *China Commun.*, vol. 21, no. 9, pp. 276–291, Sep. 2024.
[31] Z. Lin et al., "Refracting RIS-aided hybrid satellite-terrestrial relay networks: Joint beamforming design and optimization," *IEEE Trans. Aerosp. Electron. Syst.*, vol. 58, no. 4, pp. 3717–3724, Aug. 2022.
[32] K. Guo, M. Wu, X. Li, Z. Lin, and T. A. Tsiftsis, "Joint trajectory and beamforming optimization for federated DRL-aided space-aerial-terrestrial relay networks with RIS and RSMA," *IEEE Trans. Wireless Commun.*, vol. 23, no. 12, pp. 18456–18471, Dec. 2024.
[33] L. Schulthess, T. Salzmann, C. Vogt, and M. Magno, "A LoRa-based energy-efficient sensing system for urban data collection," in *Proc. Int. Workshop Adv. Sensors Interfaces (IWASI)*, 2023, pp. 69–74.
[34] R. M. Colombo, A. Mahmood, E. Sisinni, P. Ferrari, and M. Gidlund, "Low-cost SDR-based tool for evaluating LoRa satellite communications," in *Proc. IEEE Int. Symp. Meas. Netw. (MN)*, 2022, pp. 1–6.
[35] J. Petäjäjärvi, K. Mikhaylov, M. Pettissalo, J. Janhunen, and J. H. Iinatti, "Performance of a low-power wide-area network based on LoRa technology: Doppler robustness, scalability, and coverage," *Int. J. Distrib. Sensor Netw.*, vol. 13, no. 3, p. 16, 2017.
[36] Y. Li, S. Han, L. Yang, F.-Y. Wang, and H. Zhang, "LoRa on the move: Performance evaluation of LoRa in V2X communications," in *Proc. IEEE Intell. Veh. Symp. (IV)*, 2018, pp. 1107–1111.
[37] A. Doroshkin, A. Zadorozhny, O. Kus, V. Prokopyev, and Y. Prokopyev, "Laboratory testing of LoRa modulation for CubeSat radio communications," in *Proc. MATEC Web Conf.*, vol. 158, 2018, p. 1008.
[38] "TinyGS: A collaborative satellite ground station network," TinyGS. Accessed: Feb. 7, 2025. [Online]. Available: https://tinygs.com/
[39] A. M. Zadorozhny et al., "First flight-testing of LoRa modulation in satellite radio communications in low-earth orbit," *IEEE Access*, vol. 10, pp. 100006–100023, 2022.
[40] G. Colavolpe, T. Foggi, M. Ricciulli, Y. Zanettini, and J.-P. Mediano-Alameda, "Reception of LoRa signals from LEO satellites," *IEEE Trans. Aerosp. Electron. Syst.*, vol. 55, no. 6, pp. 3587–3602, Dec. 2019.
[41] S. Mukhamadiev, E. Rogozhnikov, and E. Dmitriyev, "Compensation of the frequency offset in communication systems with LoRa modulation," *Symmetry*, vol. 14, no. 4, p. 747, 2022. [Online]. Available: https://www.mdpi.com/2073-8994/14/4/747
[42] J. Kang et al., "Regression based pilot design for doppler effect estimation and compensation in LEO satellite communication with LoRa," in *Proc. 27th Asia Pacific Conf. Commun. (APCC)*, 2022, pp. 631–632.
[43] M. Asad Ullah, K. Mikhaylov, and H. Alves, "An overview of direct-to-satellite IoT: Opportunities and open challenges," in *Proc. IEEE 9th World Forum Internet Things (WF-IoT)*, 2023, pp. 1–8.
[44] M. A. Ullah, A. Yastrebova, K. Mikhaylov, M. Höyhtyä, and H. Alves, "Situational awareness for autonomous ships in the arctic: MMTC direct-to-satellite connectivity," *IEEE Commun. Mag.*, vol. 60, no. 6, pp. 32–38, Jun. 2022.
[45] K. Lin, M. A. Ullah, H. Alves, K. Mikhaylov, and T. Hao, "Subterranean mMTC in remote areas: Underground-to-satellite connectivity approach," *IEEE Commun. Mag.*, vol. 61, no. 5, pp. 136–142, May 2023.
[46] "LoRa® modem Doppler immunity," Datasheet AN1200.80-Rev. 1.0, Semtech Corp., Camarillo, CA, USA, 2023. [Online]. Available: https://www.semtech.com/products/wireless-rf/lora-connect/sx1272#documentation
[47] "Long range, low power RF transceiver 860-1000MHz with LoRa Technology," Datasheet SX1272-Rev. 4.0, Semtech Corp., Camarillo, CA, USA, 2019. [Online]. Available: https://www.semtech.com/products/wireless-rf/lora-connect/sx1272#documentation
[48] T. Ameloot, M. Moeneclaey, P. Van Torre, and H. Rogier, "Characterizing the impact of Doppler effects on body-centric LoRa links with SDR," *Sensors*, vol. 21, no. 12, p. 4049, 2021. [Online]. Available: https://www.mdpi.com/1424-8220/21/12/4049
[49] A. Fastenbauer, M. Kaneko, P. Svoboda, and M. Rupp, "Impact of elevation angle on multi-beam LEO satellite communication systems," *IEEE Access*, vol. 13, pp. 71723–71737, 2025.
[50] A. Al-Hourani and B. Al Homssi, "Doppler shift distribution in satellite constellations," *IEEE Commun. Lett.*, vol. 28, no. 9, pp. 2131–2135, Sep. 2024.
[51] M. A. Ullah et al., "Extending the LoRa direct-to-satellite limits: Doppler shift pre-compensation," *IEEE Open J. Commun. Soc.*, vol. 6, pp. 2256–2273, 2025.

JAMIL FARHAT received the B.Sc., M.Sc., and D.Sc. degrees in electrical engineering from the Federal University of Technology-Paraná, Curitiba, Brazil, in 2013, 2015, and 2018, respectively, where he has been a Professor with the Department of Electronics since 2023. His research interests include wireless communications, multiple-access strategies, machine-type communications, and physical-layer security. He serves as an Associate Editor for IEEE INTERNET OF THINGS JOURNAL.

GIANNI PASOLINI (Member, IEEE) is an Associate Professor with the Department of Electrical, Electronic and Information Engineering, University of Bologna, where he has been teaching various courses in the field of telecommunications since 2003. Throughout his career, he has actively participated in several European initiatives focused on wireless communications, including COST actions and Networks of Excellence. His research interests encompass wireless communication systems, Internet of Things, digital signal processing, and THz communications. He serves as an Associate Editor for IEEE OPEN JOURNAL OF THE COMMUNICATIONS SOCIETY. He served as a member of the Organizing Committee for several IEEE conferences. He is one of the founding members of the "National Laboratory of Wireless Communications - Wilab" of the National Inter-University Consortium for Telecommunications, Italy.

ENRICO PAOLINI (Senior Member, IEEE) received the Dr.Ing. degree (summa cum laude) in telecommunications engineering and the Ph.D. degree in electrical engineering from the University of Bologna, Italy, in 2003 and 2007, respectively. While working toward the Ph.D. degree, he was a Visiting Research Scholar with the Department of Electrical Engineering, University of Hawai'i at Manoa, Honolulu, HI, USA. He was a Visiting Scientist with the Institute of Communications and Navigation, German Aerospace Center in 2012 and 2014, respectively, under DLR-DAAD Fellowships. He is currently an Associate Professor with the Department of Electrical, Electronic, and Information Engineering, University of Bologna. His research interests include digital communication systems, error correcting codes, massive multiple access protocols, and detection and tracking in radar systems. He served as the Co-Chair for the ICC 2014, ICC 2015, and ICC 2016 Workshop on Massive Uncoordinated Access Protocols, the VTC 2019-Fall Workshop on Small Data Networks, the 2025 and the 2018 IEEE European School of Information Theory, and the 2020 IEEE Information Theory Workshop. He served as the TPC Co-Chair for the IEEE GLOBECOM 2022–CT and the IEEE GLOBECOM 2019–CT. He is a Past Chair of the ITSoc Italy Section Chapter and the Chair of the IEEE ComSoc Radio Communications Committee. He was an Editor of IEEE COMMUNICATIONS LETTERS from 2012 to 2015 and the IEEE TRANSACTIONS ON COMMUNICATIONS (in coding and information theory) from 2015 to 2020.

MUHAMMAD ASAD ULLAH (Member, IEEE) received the master's and Ph.D. (with Distinction) degrees from the University of Oulu, Finland, in 2020 and 2024, respectively. He is a Senior Scientist with the VTT Technical Research Center of Finland Ltd., Espoo, Finland. From 2018 to 2023, he was with the 6G Flagship, Centre for Wireless Communications, University of Oulu. In 2022, he was a Visiting Researcher with the University of Bologna, Italy, and a Ph.D. Student with Nokia, Finland. In 2022, he was a Finalist in the Millennium Young Scientist Contest, organized by Technology Academy Finland as part of the Millennium Innovation Forum. His technical expertise includes measurements, analytical, and simulation modeling of wireless communications systems, with a particular focus on nonterrestrial networks and aeronautical telecommunication networks.

RICHARD DEMO SOUZA (Senior Member, IEEE) received the B.Sc. and D.Sc. degrees in electrical engineering from the Federal University of Santa Catarina (UFSC), Brazil, in 1999 and 2003, respectively. From 2004 to 2016, he was with the Federal University of Technology-Paraná, Brazil. Since 2017, he has been with UFSC, where he is a Professor with the Department of Electrical and Electronics Engineering. His research interests include wireless communications and signal processing. He has served as an Editor or an Associate Editor for *SBrT Journal of Communications and Information Systems*, IEEE COMMUNICATIONS LETTERS, the IEEE TRANSACTIONS ON VEHICULAR TECHNOLOGY, the IEEE TRANSACTIONS ON COMMUNICATIONS, and IEEE INTERNET OF THINGS JOURNAL. He supervised the recipient of the 2014 Best Ph.D. Thesis in Electrical Engineering in Brazil and a co-recipient of the 2016 Research Award from the Cuban Academy of Sciences.

Coordenação de Aperfeiçoamento de Pessoal de Nível Superior (CAPES) - ROR identifier: 00x0ma614